

Turbulent Flow in a Converging-Diverging Nozzle

AEROSP 525 Final Project

Jake Lancaster, Sukhyeon Lim, Alex Kerlee

April 30, 2025

1 Introduction

Turbulent flow in converging-diverging channels, which appears in propulsion nozzles, diffusers or wind tunnels, is the case of both fundamental and practical interests. Regions of high shear, adverse pressure gradients, and potential flow separation accompanied with this flow pose significant challenges to turbulence modeling. Although Direct Numerical Simulation DNS provides high-fidelity data, it is computationally prohibitive for most practical applications. Reynolds-Averaged Navier-Stokes RANS with turbulence modeling is commonly used to predict such flows, yet its performance varies depending on the flow features and turbulence models. This project aims to compare the performance of several widely used turbulence models $k-\varepsilon$, $k-\omega$, and SST in simulating a 2-D converging-diverging channel using ANSYS CFX. The performance of each turbulence model will be verified against benchmark DNS data from NASA's turbulence database and compared with previous research. Based on these processes, it is expected to quantify the performance and the accuracy of each turbulence model with RANS.

2 Methods

2.1 Literature Review

The direct numerical simulation (DNS) of turbulent flow through a two-dimensional converging-diverging channel at a Reynolds number of 12,600 serves as our benchmark for validating the turbulence models we run through ANSYS CFX, especially in flows involving adverse pressure gradients and separation. Conducted by J.-P. Laval and collaborators, this simulation is made available through NASA's Turbulence Modeling Resource and offers a comprehensive dataset for researchers. The study focuses on incompressible, fully developed turbulent channel flow in a converging-divergent nozzle, allowing the flow to undergo smooth geometric contractions and expansions, which generates flow phenomena such as separation, reattachment, and varying turbulence intensity. The Reynolds number is based on the channel half-height, maximum inlet velocity, and kinematic viscosity, ensuring a realistic representation of wall-bounded turbulence with strong pressure gradient effects.

To resolve the wide range of spatial and temporal scales present in turbulent flow, the simulation employs a highly refined structured mesh. The full-resolution computational grid contains approximately 511 million points, with 576 cells in the spanwise direction and 2304 in the streamwise direction, ensuring that turbulent structures and boundary layer features are well-resolved. For easier post-processing and data handling, a coarsened version of the dataset is also provided, with only half the data points in each direction. The structured nature of the grid simplifies the application of finite-difference methods used in the DNS and supports detailed analysis of mean and fluctuating quantities.

The available dataset includes time-averaged mean flow variables, Reynolds stress components, and the full budget terms of the momentum equations. These budget terms encompass production, dissipation, turbulent transport, and viscous diffusion, with dissipation and diffusion values reported without the viscosity factor

$(\nu = 1/12,600)$.

Graphs of the NASA data will be interspersed throughout the report for comparison to the results we have obtained.

2.2 Geometry and CAD Modeling

The CAD model was developed using Solidworks, a 3D computer-aided design (CAD) software provided by the University of Michigan for student use. It can be used to create detailed parts, assemblies, and technical drawings as well as design, simulate, and prepare products for manufacturing. For this analysis, it was used to generate a CAD model based on the geometry provided by NASA.

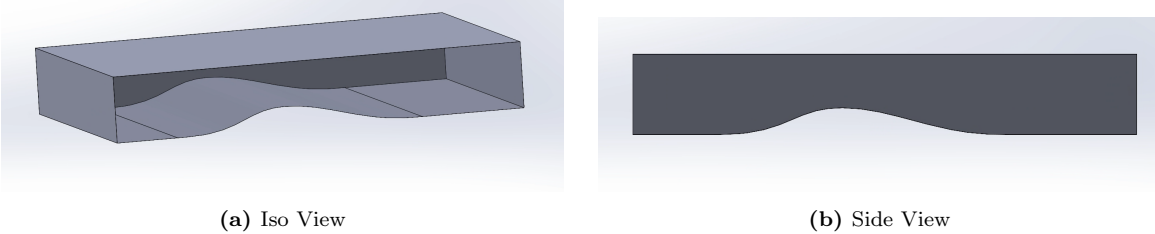


Figure 1: CAD Model of CD Nozzle Volume

The model the team used was generated using NASA geometry data and generating a 2D curve. The curve is then extruded and converted into a volume to create inlet, outlets, and wall. According to the NASA dataset there should be a hill crest at approximately 2/3 units high, at location near $x=5.21564$ and the channel half-height = $h = 1$ unit full channel height = $2h$. The geometry was scaled to match the Reynolds number of 12,600 while maintaining the bulk velocity at the channel inlet as 1 m/s. The half channel height of the geometry for CFD was set as 0.198 m, the channel width as 1.98 m, and the channel length as 2.49 m.

$$Re = \frac{U_{max}h}{\nu} = 12,600$$

2.3 Mesh Generation: ANSYS CFX

To generate a mesh for the simulation in ANSYS CFX, the CAD model of the converging-diverging nozzle, created in SolidWorks using data from NASA, was imported into CFX. CFX's native meshing tools were then used to create a computational grid suitable for the problem. The meshing process begins by defining the geometry of the nozzle, ensuring that the mesh adequately resolves critical regions, such as the throat and the nozzle exit, where flow gradients and potential shock waves occur. The meshing tools allow for automatic refinement of the mesh near walls and regions of high flow gradients. Depending on the flow characteristics, such as compressibility or boundary layer behavior, mesh in CFX can be either structured or unstructured, with the ability to use hybrid meshes that combine both types. For the purposes of this project, we used a structured mesh. Once the mesh is generated, boundary conditions, such as the inlet velocity, outlet pressure, and wall conditions, are applied. After completing the mesh generation, the model is ready for simulation, where CFX solves the governing equations to simulate the flow characteristics through the nozzle, capturing important phenomena like shock formation, expansion waves, and flow separation.

Mesh grid sizing is fundamental to the quality and reliability of CFD simulations, as the mesh defines how the continuous flow domain is discretized for numerical analysis. In structured grids, the domain is divided into a logically ordered arrangement of cells, which simplifies implementation and improves numerical accuracy, especially in flows with smooth geometries like converging-diverging nozzles. The resolution of the mesh, whether coarse or fine, determines how well gradients in flow variables such as velocity, pressure, and temperature can be captured. A coarse grid offers lower computational cost and faster simulations but may fail to resolve critical features such as boundary layers, shock waves, or flow separation. In contrast, a fine

grid increases the ability to capture these features with higher fidelity, allowing for more accurate predictions of complex flow phenomena, but at the expense of greater computational time and resources. Choosing an appropriate grid size involves balancing accuracy requirements with computational constraints and often requires a grid sensitivity or convergence study to ensure that the numerical solution is independent of the mesh resolution. Below are images of the two meshes (coarse uniform and fine variable) used in CFX to analyze the data.

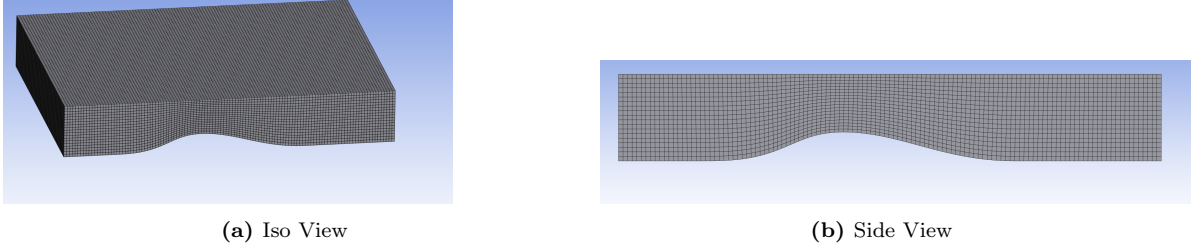


Figure 2: Coarse Mesh Images

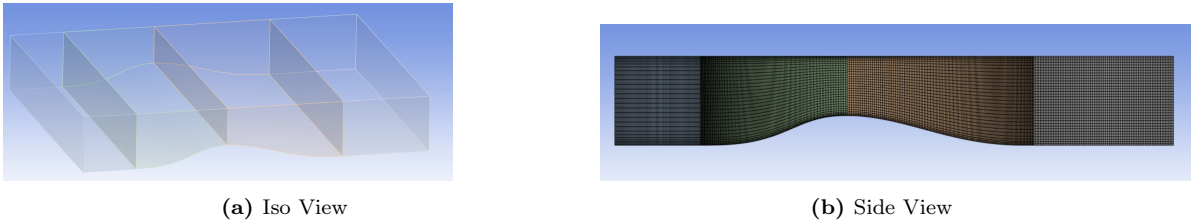


Figure 3: Fine Mesh Images

Mesh	Number of elements	Mesh type
Coarse Mesh	230 000	Uniform
Fine Mesh	1.5 million	Variable

Table 1: Summary of mesh resolutions.

2.4 Finite Volume Solver - Algebraic Multigrid: ANSYS CFX

ANSYS CFX is a computational fluid dynamics CFD software package designed for the simulation of fluid flow, heat transfer, and related physical phenomena. It discretizes the Navier–Stokes equations using the finite volume method on structured, unstructured, or hybrid grids. CFX employs a fully coupled, fully implicit solution algorithm, solving continuity, momentum, energy, and turbulence equations simultaneously at each iteration. Linear systems arising from the discretization are typically solved using Krylov subspace methods such as GMRES or BiCGSTAB, with algebraic multigrid AMG techniques used to improve convergence rates. CFX supports a variety of turbulence models, including $k-\varepsilon$, $k-\omega$, SST, and Reynolds stress models, depending on the complexity of the flow. For a two-dimensional converging-diverging nozzle problem, CFX can simulate compressible, potentially supersonic flow by applying appropriate inlet and outlet boundary conditions, capturing phenomena such as isentropic expansion, shock formation, and boundary layer effects along the nozzle walls.

2.5 RANS Turbulence Models

2.5.1 Standard k- ε Model [3]

One of the most notable turbulence models is the k- ε Model.

$$\frac{\partial k}{\partial t} + \langle U_j \rangle \frac{\partial k}{\partial x_j} = - \langle u_i u_j \rangle \frac{\partial \langle U_i \rangle}{\partial x_j} - \varepsilon + \frac{\partial}{\partial x_j} \left[\left(\nu + \frac{\nu_T}{\sigma_k} \right) \frac{\partial k}{\partial x_j} \right], \quad (1)$$

$$\frac{\partial \varepsilon}{\partial t} + \langle U_j \rangle \frac{\partial \varepsilon}{\partial x_j} = - C_{\varepsilon 1} \frac{\varepsilon}{k} \langle u_i u_j \rangle \frac{\partial \langle U_i \rangle}{\partial x_j} - C_{\varepsilon 2} \frac{\varepsilon^2}{k} + \frac{\partial}{\partial x_j} \left[\left(\nu + \frac{\nu_T}{\sigma_\varepsilon} \right) \frac{\partial \varepsilon}{\partial x_j} \right], \quad (2)$$

$$\nu_T = C_\mu \frac{k^2}{\varepsilon}, \quad (3)$$

$$\langle u_i u_j \rangle = -2 \nu_T \langle S_{ij} \rangle + \frac{2}{3} k \delta_{ij}. \quad (4)$$

where the Boussinesq assumption yields:

$$\langle S_{ij} \rangle = \frac{1}{2} \left(\frac{\partial \langle U_i \rangle}{\partial x_j} + \frac{\partial \langle U_j \rangle}{\partial x_i} \right).$$

In order to run the k- ε solver in ANSYS, the software requires input of TKE (turbulent kinetic energy) and turbulence eddy dissipation. The input values were derived using the below process with NASA DNS data.

$$k(x, y) = \frac{1}{2} (\langle uu \rangle + \langle vv \rangle + \langle ww \rangle) \quad (5)$$

$$\bar{k}(x) = \frac{1}{2h} \int_0^{2h} k(x, y) dy \quad (6)$$

$$\varepsilon(x, y) = 2\nu \left(\left\langle \frac{\partial u}{\partial x} \frac{\partial u}{\partial x} \right\rangle + \left\langle \frac{\partial u}{\partial x} \frac{\partial u}{\partial y} \right\rangle + \left\langle \frac{\partial u}{\partial y} \frac{\partial u}{\partial x} \right\rangle \right) \quad (7)$$

$$\bar{\varepsilon}(x) = \frac{1}{2h} \int_0^{2h} \varepsilon(x, y) dy \quad (8)$$

$$k_{inlet} = \bar{k}(x_{inlet}), \quad \varepsilon_{inlet} = \bar{\varepsilon}(x_{inlet}) \quad (9)$$

2.5.2 Standard k- ω Model

The most popular two-equation alternative is the k- ω model (Wilcox 1993; Menter 1993), in which the ε transport equation is replaced by one for the specific dissipation rate ω , loosely defined as the inverse turbulence timescale ($\omega \propto \varepsilon/k$) [2].

A widely used Wilcox (1993) formulation sets

$$\nu_T = \frac{k}{\omega},$$

and solves the scalar transport equations

$$\frac{\partial k}{\partial t} + \langle U_j \rangle \frac{\partial k}{\partial x_j} = 2 \nu_T |S|^2 - C_\mu k \omega + \frac{\partial}{\partial x_j} \left[\left(\nu + \frac{\nu_T}{\sigma_k} \right) \frac{\partial k}{\partial x_j} \right], \quad (7.7)$$

$$\frac{\partial \omega}{\partial t} + \langle U_j \rangle \frac{\partial \omega}{\partial x_j} = -C_{\omega 1} |S|^2 - C_{\omega 2} \omega^2 + \frac{\partial}{\partial x_j} \left[\left(\nu + \frac{\nu_T}{\sigma_\omega} \right) \frac{\partial \omega}{\partial x_j} \right]. \quad (7.8)$$

Here the constants ($C_\mu, C_{\omega 1}, C_{\omega 2}, \sigma_k, \sigma_\omega$) are calibrated analogously to the k- ε model.

In order to run the k- ω solver in ANSYS, the software requires input of TKE (turbulent kinetic energy) and turbulence eddy frequency. The input values were derived using the below process with NASA DNS data.

$$k(x, y) = \frac{1}{2} (\langle uu \rangle + \langle vv \rangle + \langle ww \rangle) \quad (10)$$

$$\bar{k}(x) = \frac{1}{2h} \int_0^{2h} k(x, y) dy \quad (11)$$

$$\varepsilon(x, y) = 2\nu \left(\left\langle \frac{\partial u}{\partial x} \frac{\partial u}{\partial x} \right\rangle + \left\langle \frac{\partial u}{\partial x} \frac{\partial u}{\partial x} \right\rangle + \left\langle \frac{\partial u}{\partial x} \frac{\partial u}{\partial x} \right\rangle \right) \quad (12)$$

$$\nu_T = C_\mu \frac{k^2}{\varepsilon} = \frac{k}{\omega} \quad (13)$$

$$\omega(x, y) = \frac{\varepsilon(x, y)}{C_\mu k(x, y)} \quad (14)$$

$$\bar{\omega}(x) = \frac{1}{2h} \int_0^{2h} \omega(x, y) dy \quad (15)$$

$$k_{inlet} = \bar{k}(x_{inlet}), \quad \omega_{inlet} = \bar{\omega}(x_{inlet}) \quad (16)$$

The $k-\omega$ model offers:

- Better prediction under adverse pressure gradients than $k-\varepsilon$.
- Increased numerical robustness for integration up to a no-slip wall.
- Closed-form leading-order behavior of ω at a solid boundary.
- Asymptotic inconsistency of TKE near a wall (mitigated in some low-Re variants).
- Sensitivity to free-stream ω boundary values outside the shear layer

2.5.3 $k-\omega$ SST Model

The Shear-Stress Transport (SST) model blends the robust near-wall behavior of the $k-\omega$ formulation with the free-stream insensitivity of the $k-\varepsilon$ model. This hybrid approach uses two transport equations—one for the turbulent kinetic energy k and one for the specific dissipation rate ω —augmented by blending functions to switch between the two closures [4].

$$\frac{\partial k}{\partial t} + U_j \frac{\partial k}{\partial x_j} = P_k - \beta^* k \omega + \frac{\partial}{\partial x_j} \left[(\nu + \sigma_k \nu_T) \frac{\partial k}{\partial x_j} \right], \quad (17)$$

$$\frac{\partial \omega}{\partial t} + U_j \frac{\partial \omega}{\partial x_j} = \alpha \frac{\omega}{k} P_k - \beta \omega^2 + \frac{\partial}{\partial x_j} \left[(\nu + \sigma_\omega \nu_T) \frac{\partial \omega}{\partial x_j} \right] + 2(1 - F_1) \frac{\sigma_{\omega 2}}{\omega} \frac{\partial k}{\partial x_j} \frac{\partial \omega}{\partial x_j}, \quad (18)$$

where the eddy viscosity is defined as

$$\nu_T = \frac{a_1 k}{\max(a_1 \omega, S F_2)},$$

with $P_k = \nu_T S^2$ and $S = \sqrt{2 S_{ij} S_{ij}}$.

The two blending functions F_1 and F_2 control the transition between the $k-\omega$ and $k-\varepsilon$ formulations:

$$F_1 = \tanh \left[\min(\max(A_1, A_2), A_3) \right], \quad F_2 = \tanh \left[\max(B_1, B_2) \right],$$

where $F_1 \rightarrow 1$ in near-wall regions (activating the $k-\omega$ mode) and $F_1 \rightarrow 0$ away from walls (activating the $k-\varepsilon$ mode). The arguments A_i, B_i are algebraic functions of k, ω, ν , and local distance to the wall.

In CFX, the SST model uses the default coefficient values above. Inlet boundary conditions for k and ω were specified via turbulence intensity and length scale, and under-relaxation factors were adjusted (typically

Table 2: SST model constants

Constant	Value
a_1	0.31
β^*	0.09
β_1	0.075
β_2	0.0828
σ_{k1}	0.85
$\sigma_{\omega 1}$	0.50
σ_{k2}	1.00
$\sigma_{\omega 2}$	0.856

0.8 for momentum and 0.7 for turbulence equations) to ensure stable convergence. The algebraic multigrid solver with full coupling was employed to accelerate residual reduction.

The SST model accurately predicts flow separation and adverse pressure-gradient effects, while maintaining robustness in free-stream regions. However, it remains sensitive to the prescribed free-stream value of ω , necessitating careful boundary condition specification.

2.6 Mesh Grid Size Comparison

2.6.1 NASA Grid Size

The original data from NASA had a structured grid as well. These results are from a grid with approximately 511 million grid points, covering a spanwise extent of π 3.14159... with 576 cells in the spanwise direction. The files with field results on one plane of the full grid 385 x 2304 are very large, so for convenience the field results were also given in files containing only every other point 193 x 1152.

2.6.2 Coarse Mesh

The coarse mesh was generated with a grid of 19 x 120. This coarse mesh, including the 3D component, had a total of 230,000 elements uniformly spaced in the x-direction. It can be seen in the figure below that the change in spacing in the y-direction is relatively consistent throughout the mesh with a dip in the mesh spacing near the bump where the cells are more compressed and have a smaller cell variation.

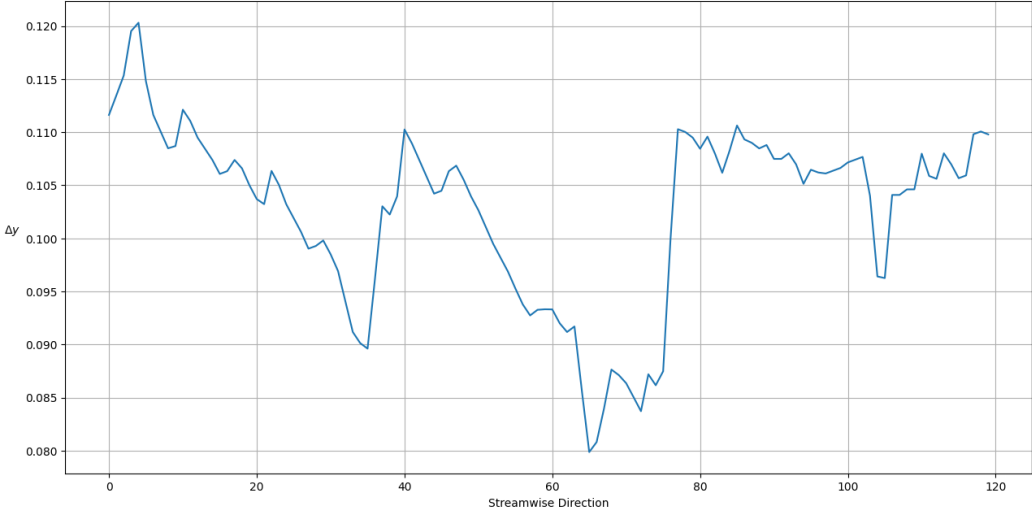


Figure 4: Δy Variation for the Coarse Mesh

2.6.3 Fine Mesh

The fine mesh was generated with variable grid spacing of 21 x 25, 33 x 80, 33 x 120, and 39 x 30. This fine mesh, including the 3D component, had a total of 1.5 million elements. The plot below shows three sections with distinct jumps, each occurring as we shift to a new section of the variable grid. The first and fourth grid size variation are fairly consistent hovering at or below 0.02. The third Δy variation peaks much higher, around 0.07. This is counter-intuitive compared to the last grid, but this is where the most change in total channel height occurs over the longest distance in this variable grid (see Fig. 23). The same is true for the second section all though the result is much more subtle since that section of the grid spends less distance varying the channel height.

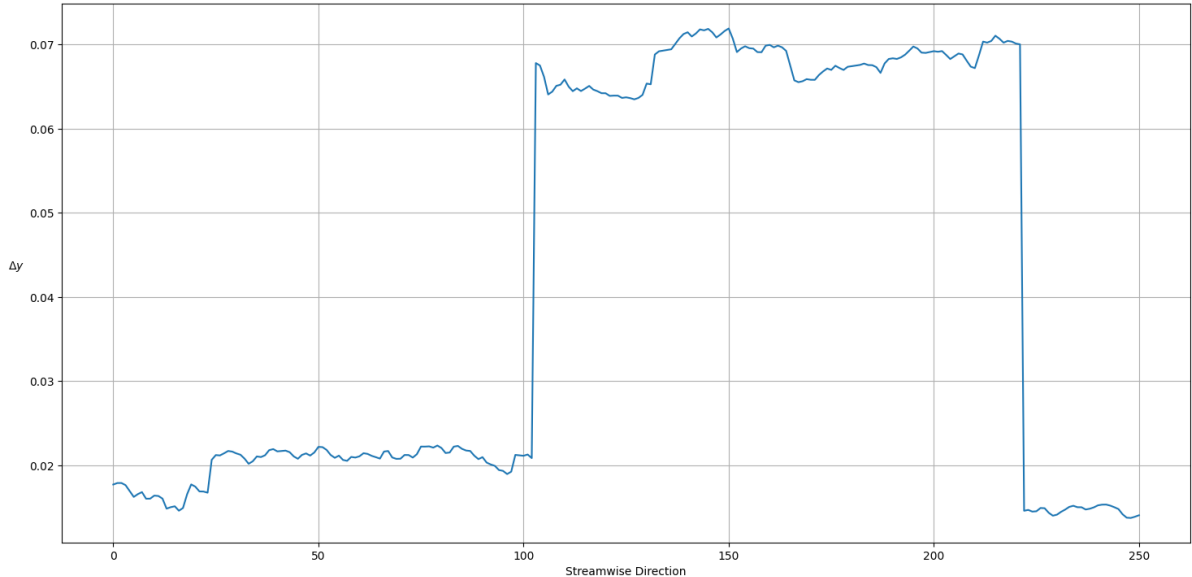


Figure 5: Δy Variation for the Fine Mesh

2.6.4 Mesh Convergence Study

Figures 6–8 present the grid-sensitivity results for the three RANS closures. In each case, the solid line denotes predictions on the fine mesh (1.5 M elements) and the dashed line the coarse mesh (230 k elements), with the vertical axis normalized to the fine-mesh peak value.

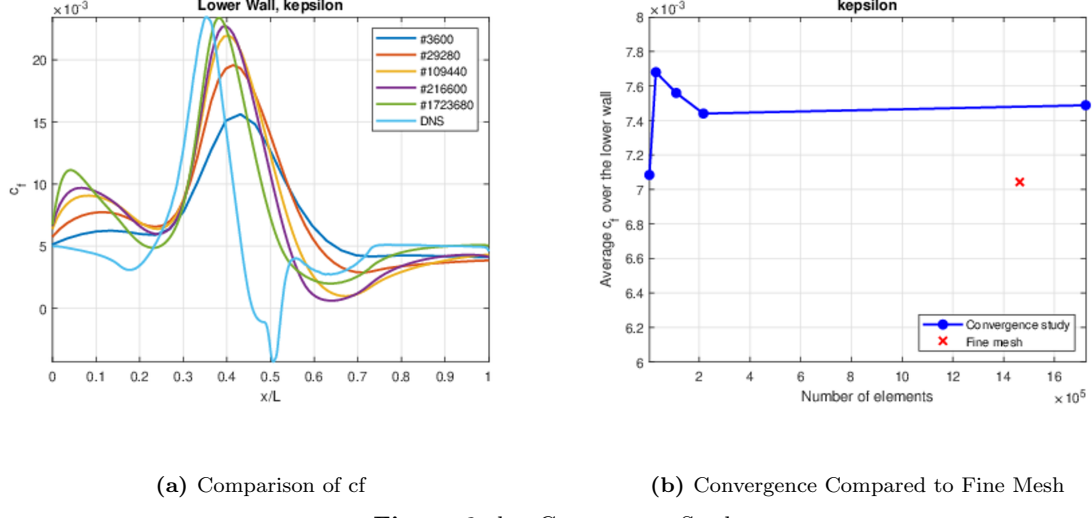


Figure 6: $k-\epsilon$ Convergence Study

Standard $k-\epsilon$ Model (Figure 6) On the coarse mesh analysis in plot 6(a), the predicted skin friction coefficient is over-predicted by all mesh sizes until the nozzle begins to converge. After the converging section separation begins to take place and the model can no longer predict the c_f with any fidelity. After the flow begins to reattach the model begins to converge, but still under-predicts the DNS data. In plot 6(b) the average c_f value converges as the number of elements increases, but slightly misses the fine mesh data average.

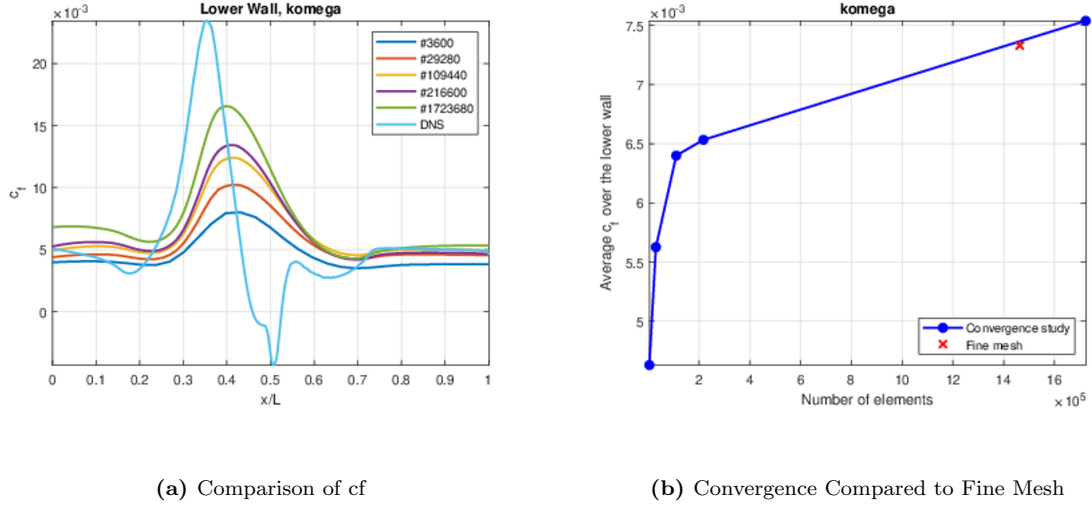


Figure 7: $k-\omega$ Convergence Study

Standard $k-\omega$ Model (Figure 7) The $k-\omega$ results exhibit intermediate mesh sensitivity. While more consistent than $k-\epsilon$ there appears to be severe underprediction in peak regions at the throat. Due to the lower mesh sensitivity, the average value in the coarse mesh agrees with the fine mesh result.

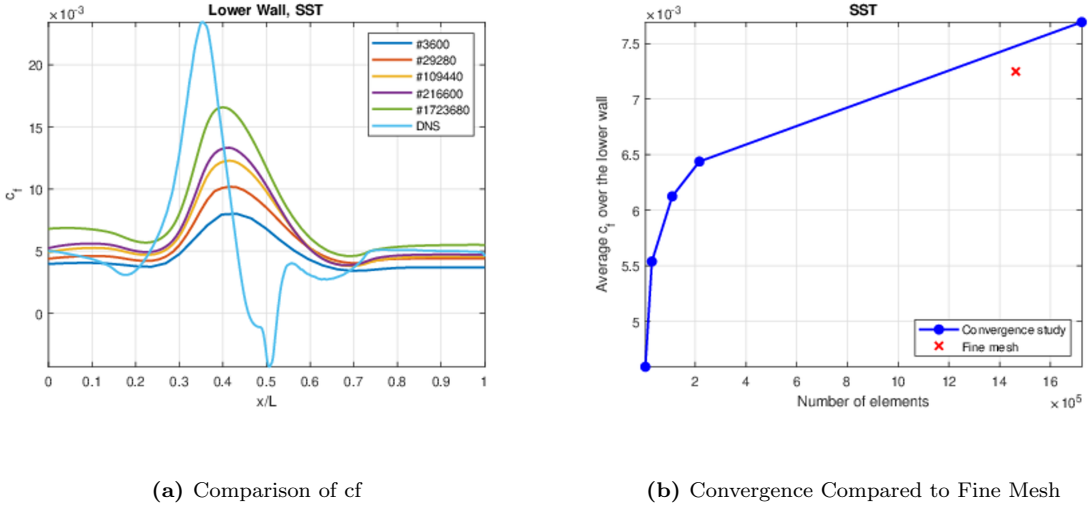


Figure 8: SST Convergence Study

SST Model (Figure 8) The SST formulation seems to have a slightly more sensitive mesh than the $k-\omega$. This can be attributed to the combination of both previous models.

Overall, the mesh convergence study confirms that at least 1.5 M elements are required to fully capture the high-gradient features in the $k-\varepsilon$ and $k-\omega$ models, whereas the SST closure yields acceptably converged results on the coarse grid. These findings justify use of the fine mesh for quantitative comparisons, while suggesting that SST may be employed with reduced computational cost when resources are limited.

3 Results

3.1 NASA Results

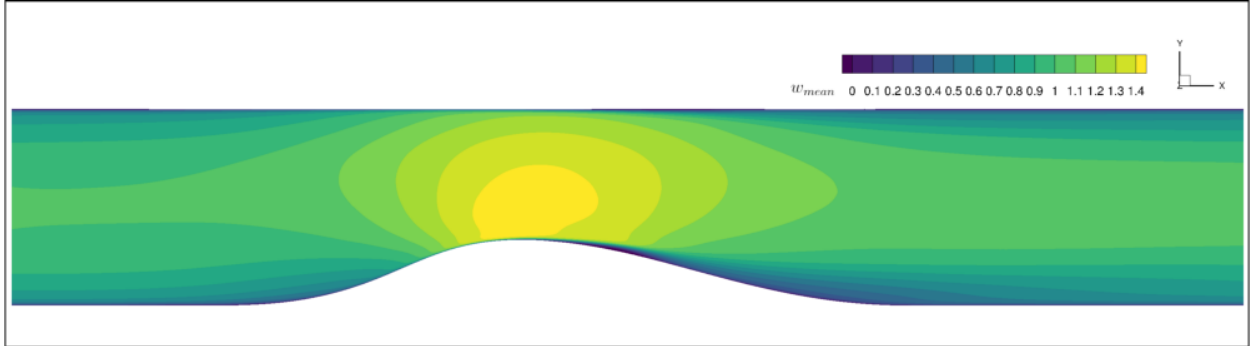


Figure 9: u_{mean} from NASA Data

The contour plot of u_{mean} in Figure 9 reveals the expected acceleration and deceleration behavior of the streamwise velocity as the flow passes through the converging-diverging nozzle. In the converging region, u_{mean} increases due to the reduction in cross-sectional area, reaching a peak just past the throat where the area is minimum. Downstream of the throat, the streamwise velocity decreases as the channel diverges and the flow expands. This trend reflects the conservation of mass in the incompressible or low-speed compressible regime. The contours also show how the boundary layers develop along the walls and interact with the geometry-induced pressure gradients, contributing to flow acceleration near the centerline and deceleration near the walls due to wall friction.

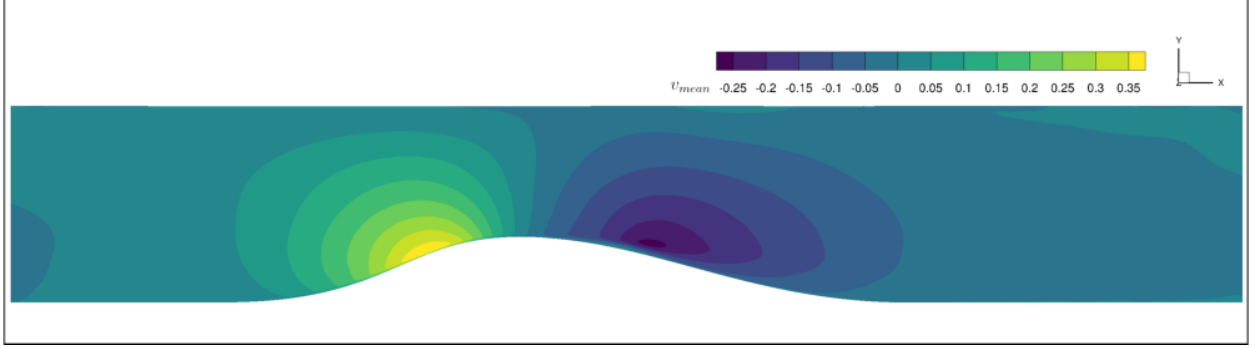


Figure 10: v_{mean} from NASA Data

In Figure 10, the v_{mean} contour plot provides insight into the wall-normal motion induced by the nozzle geometry and turbulent mixing. Upstream of the throat, there is a region of positive v_{mean} , indicating upward motion likely caused by the favorable pressure gradient and flow redirection. Just past the throat, a region of negative v_{mean} appears near the lower wall, suggesting downward motion as the flow adjusts to the diverging geometry. These opposing vertical motions are signatures of the complex secondary flows and vortex structures that arise in turbulent flows with significant curvature or area change.

The turbulent kinetic energy TKE was not provided within the NASA provided dataset. As such, we calculated it on our own in Python using the following technique:

The TKE, denoted by k , is defined as:

$$k = \frac{1}{2} \overline{u'_i u'_i} = \frac{1}{2} \left(\overline{u'^2} + \overline{v'^2} + \overline{w'^2} \right) \quad (19)$$

In two-dimensional simulations as is the case here, the spanwise component w' is not resolved, so the TKE is computed from the streamwise and wall-normal velocity fluctuations:

$$k_{2D} = \frac{1}{2} \left(\overline{u'^2} + \overline{v'^2} \right) \quad (20)$$

In the DNS data file, the dissipation terms for each Reynolds stress component are provided, specifically:

$$\varepsilon_{uu} = \text{dissipation of } \overline{u'^2} \quad (21)$$

$$\varepsilon_{uv} = \text{dissipation of } \overline{u'v'} \quad (22)$$

$$\varepsilon_{vv} = \text{dissipation of } \overline{v'^2} \quad (23)$$

The overall dissipation of TKE is approximated in 2D as the sum of the dissipation of the normal stress components:

$$\varepsilon_k = \frac{1}{2} (\varepsilon_{uu} + \varepsilon_{vv}) \quad (24)$$

Note that in this dataset, the dissipation terms are given without the viscosity factor ν , so the actual physical dissipation rate would be:

$$\varepsilon_{ij}^{\text{physical}} = \nu \cdot (\text{dissipation term from file}) \quad (25)$$

where $\nu = 1/12600$ for this case.

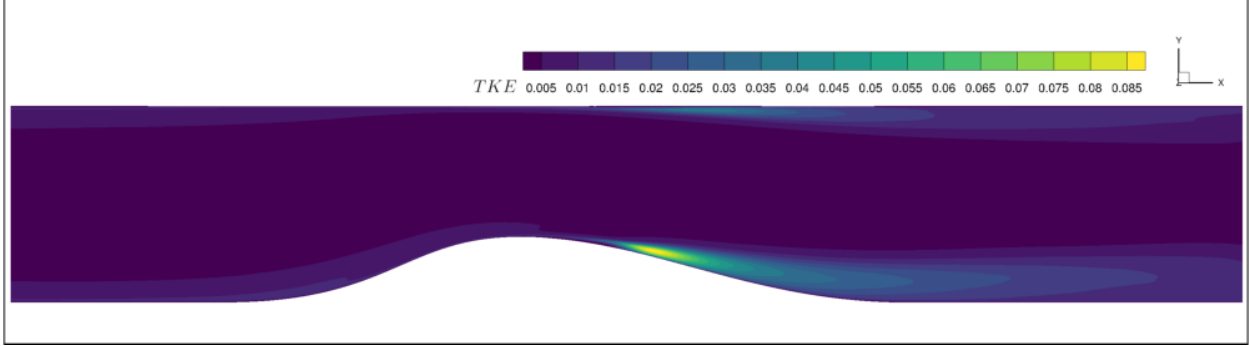


Figure 11: Turbulent Kinetic Energy from NASA Data

The TKE contour plot provides insight into where turbulence is most actively produced and sustained within the converging-diverging nozzle. As shown in the figure, TKE is relatively low throughout the domain except in the region just downstream of the throat, where a clear peak appears near the lower wall. This localized increase in TKE corresponds to the onset of flow separation or strong shear layer development due to the rapid expansion and adverse pressure gradient in the diverging section. The TKE distribution suggests enhanced turbulent mixing in this region, which is characteristic of separated or reattaching flows. Upstream of the throat, the TKE remains minimal, reflecting the stabilizing effect of favorable pressure gradients in the converging section. Overall, the plot highlights how geometric features like the nozzle shape can significantly influence turbulence generation and redistribution in internal flows.

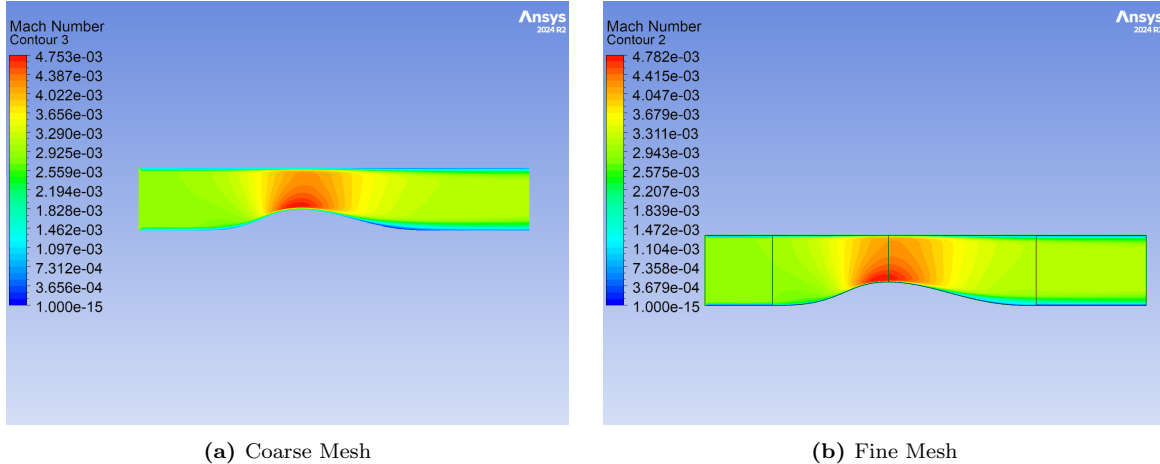
3.2 ANSYS CFX

3.2.1 $k-\varepsilon$ Simulation

This subsection evaluates the performance of the standard $k-\varepsilon$ turbulence model on both coarse and fine computational meshes. Key flow metrics—Mach-number distribution, turbulent kinetic energy, and eddy-viscosity profiles—are compared against DNS reference data to assess the impact of mesh resolution on predicted throat acceleration, shear-layer development, and downstream reattachment in separated nozzle flow. The following Variables were input for each mesh for the $k-\varepsilon$ study.

Simulation Inputs	
Fluid	Air Ideal Gas
Reference pressure	1 atm
Isothermal temperature	300 K
Reynolds number	12,600
Turbulent kinetic energy, k	0.003989
Dissipation rate, ε	0.0058

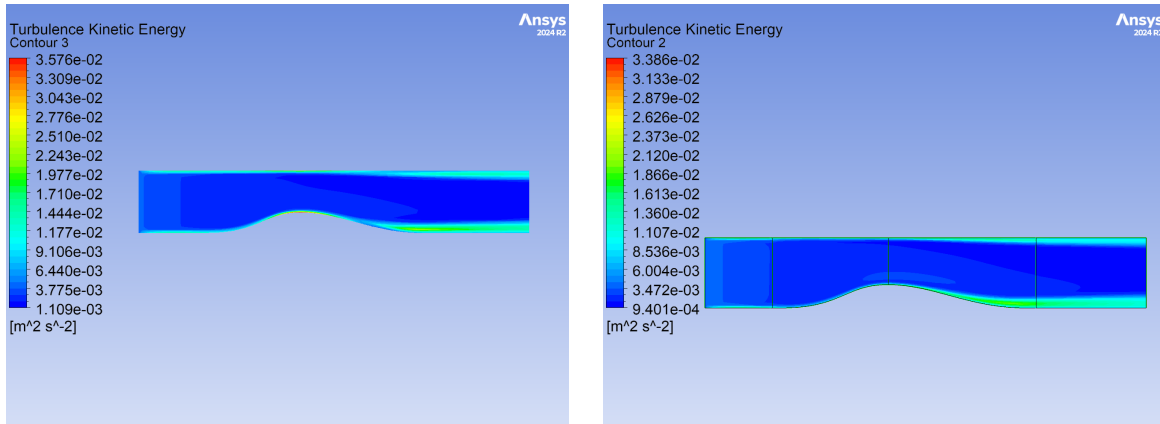
Table 3: Key parameters used in the CFD simulation.



(a) Coarse Mesh

(b) Fine Mesh

Figure 12: Mach Number Comparison



(a) Coarse Mesh

(b) Fine Mesh

(c) NASA DNS TKE

Figure 13: TKE Comparison

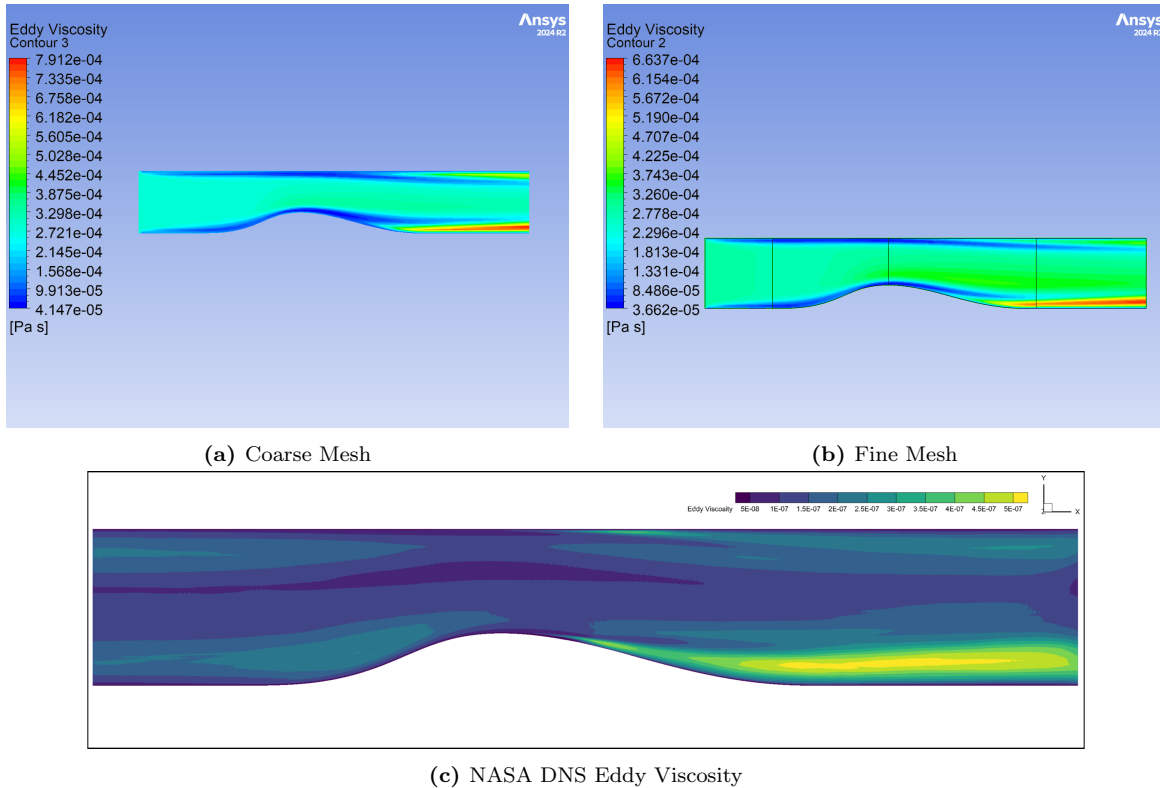


Figure 14: Eddy Viscosity Comparison

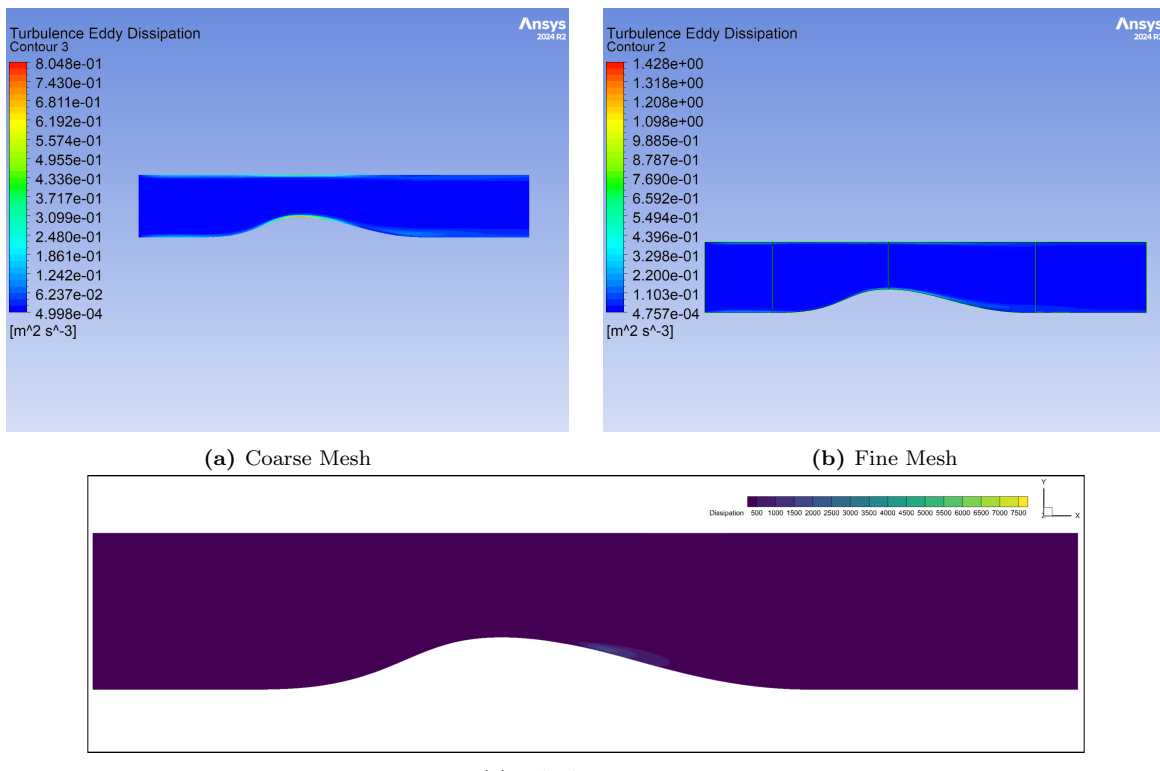


Figure 15: Turbulent Eddy Dissipation Comparison

The converging-diverging channel accelerates the flow through a throat and introduces an adverse pressure gradient in the diverging section, producing a thin separation bubble downstream of the crest near the bottom wall. Both results from coarse and fine mesh reproduce the general flow topology and follow trends observed in NASA's DNS result. Key differences arise in the resolution of velocity and turbulence gradients, and in the predicted size and intensity of the separated region.

Peak Mach numbers at the throat are nearly identical across both RANS grids. However, the fine mesh maintains the high speed core closer to the wall, while the coarse mesh disperses it into the channel interior. The upstream boundary layers are noticeably thicker on the coarse grid, indicating under predicted wall shear, unlike the thinner profile of fine mesh result.

Two meshes also show difference with TKE contours. The coarse mesh distributes moderate k across the channel core, while the fine mesh confines elevated k to a narrow region near the wall and along the separated shear layer. Even with improved resolution, the fine mesh result still under predicts peak k in the adverse pressure gradient zone by a factor of 2-3, consistent with the known limitations of isotropic eddy-viscosity models. This underestimation weakens Reynolds stresses, produces a thinner shear layer, and leads to over predicted static pressure recovery. Within the diverging section, separation and the high-shear layer are poorly captured on the coarse grid but better resolved on the fine mesh, which is close to the trend of DNS result. The eddy dissipation and eddy viscosity contours of both mesh qualitatively agree with each other but both show the discrepancy of magnitude when comparing with DNS results.

Grid resolution determines the location and shape of velocity and turbulence gradients, while the turbulence model governs their magnitude. The fine mesh aligns qualitatively with DNS flow topology, but model-form limitations still suppress k , delaying separation and reattachment.

3.2.2 $k-\omega$ Simulation

Simulation Inputs	
Fluid	Air Ideal Gas
Reference pressure	1 atm
Isothermal temperature	300 K
Reynolds number	12,600
Turbulent kinetic energy, k	0.003989
Specific dissipation rate, ω	16.3484
Jet coefficient	0.9
Separation coefficient	0.5
Near-wall coefficient	1.75

Table 4: Key input parameters for the turbulence model simulation.

The **jet coefficient** is set to 0.9. In CFX this value multiplies the production term in the turbulence equations whenever a free-jet (shear-layer) region is detected. Values below unity gently reduce turbulence production in rapidly spreading jets—damping spurious peaks in the eddy viscosity μ_t —while values closer to 1 yield a higher modeled turbulent growth rate in shear regions.

The **separation coefficient** is 0.5. It controls how aggressively the model limits μ_t under strong adverse pressure gradients or incipient separation. Lower values clamp μ_t more strongly, sharpening the separation bubble and accelerating reattachment; higher values permit more eddy viscosity, which can smear out separated zones.

The **near-wall coefficient** has a value of 1.75. This parameter modifies the length-scale damping function in the viscous sub-layer, governing how rapidly k and ω collapse toward the wall. A larger coefficient pushes the effective wall-turbulence damping zone farther from the surface, thickening the buffer layer in the y^+ profile.

Note that these are default values specified by CFX. Analysis of these coefficients and their adjustment was deemed to be outside the scope of the study.

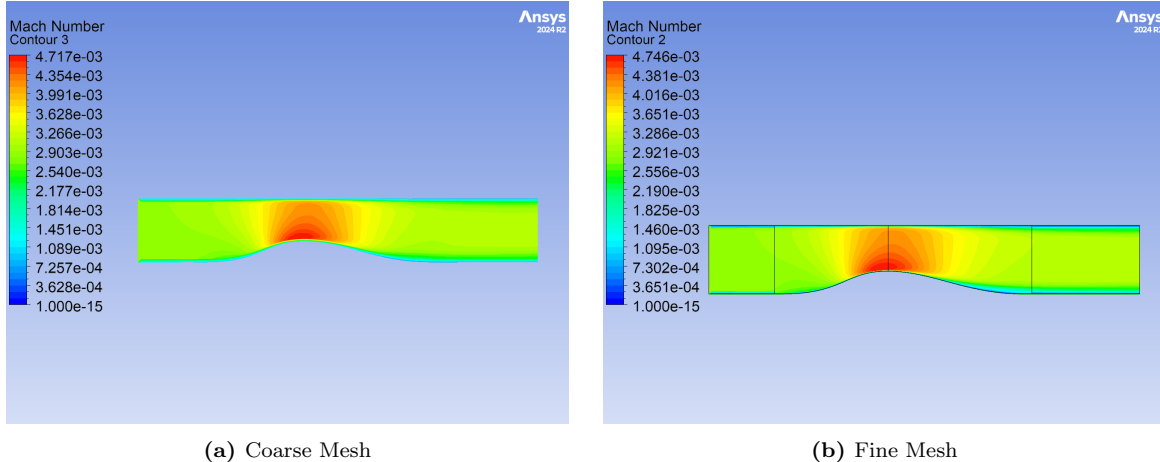


Figure 16: $k-\omega$ Mach Number Comparison

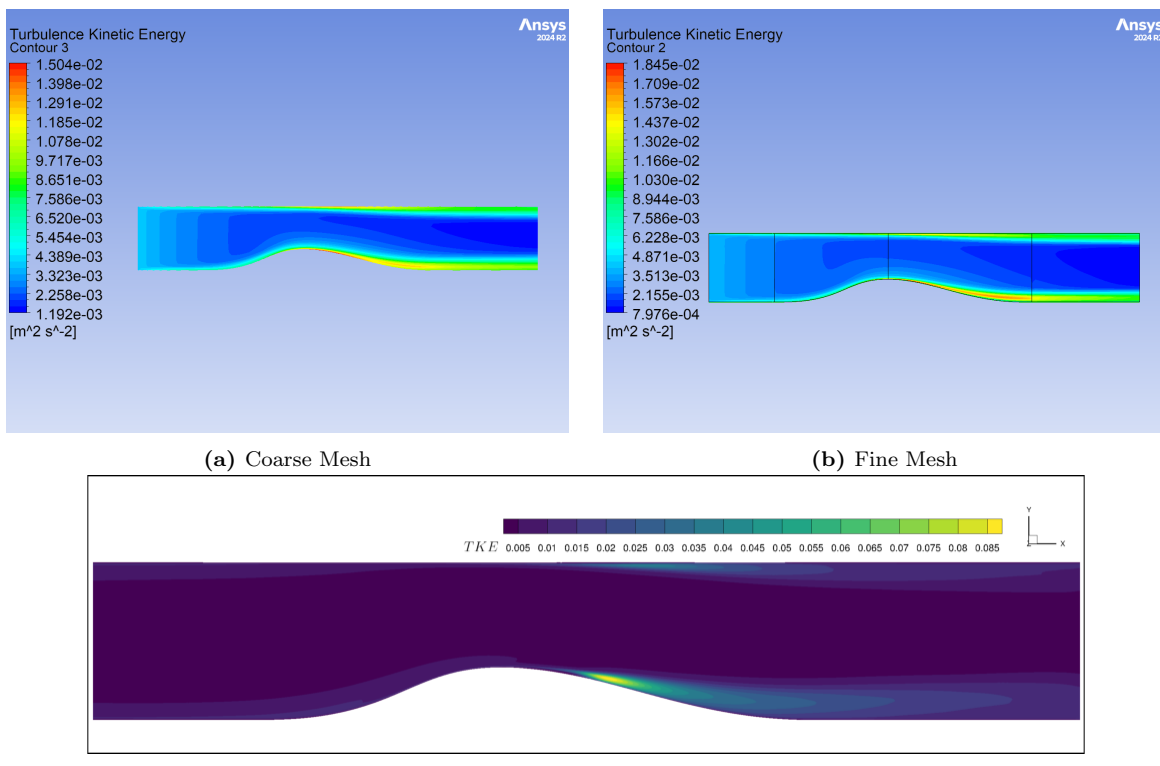


Figure 17: $k-\omega$ TKE Comparison

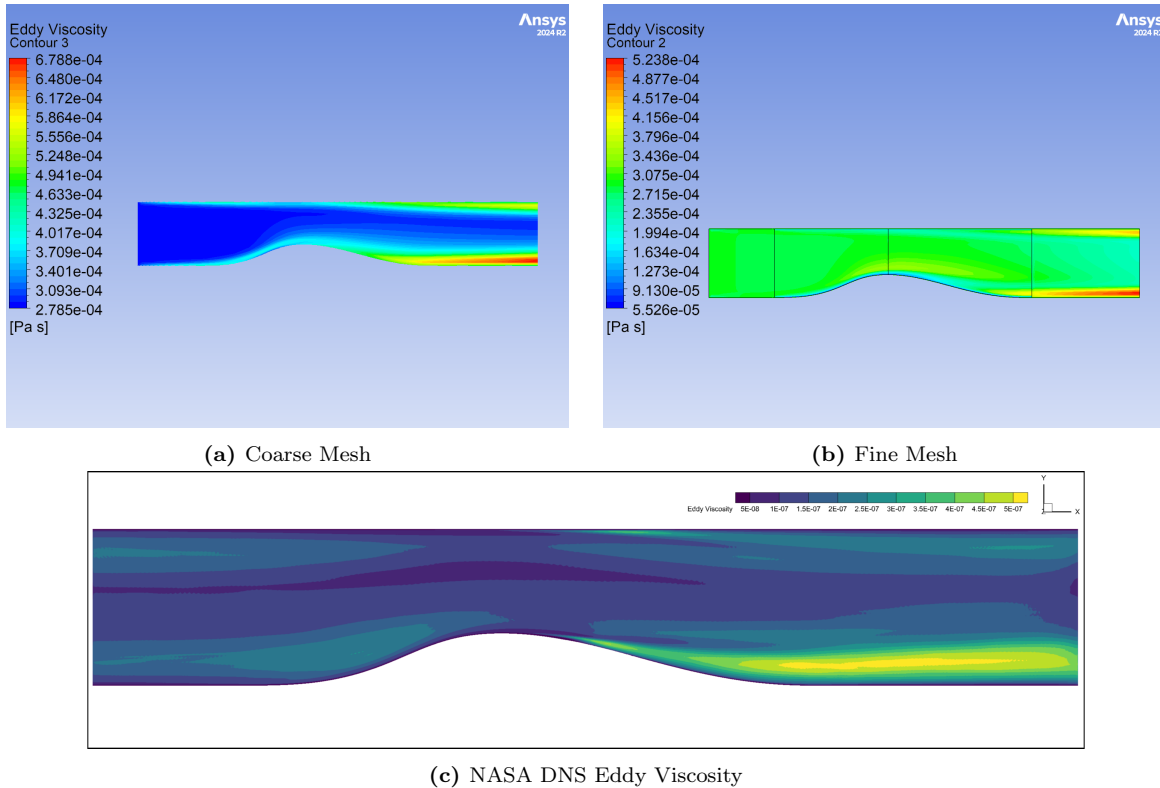


Figure 18: $k-\omega$ Eddy Viscosity Comparison

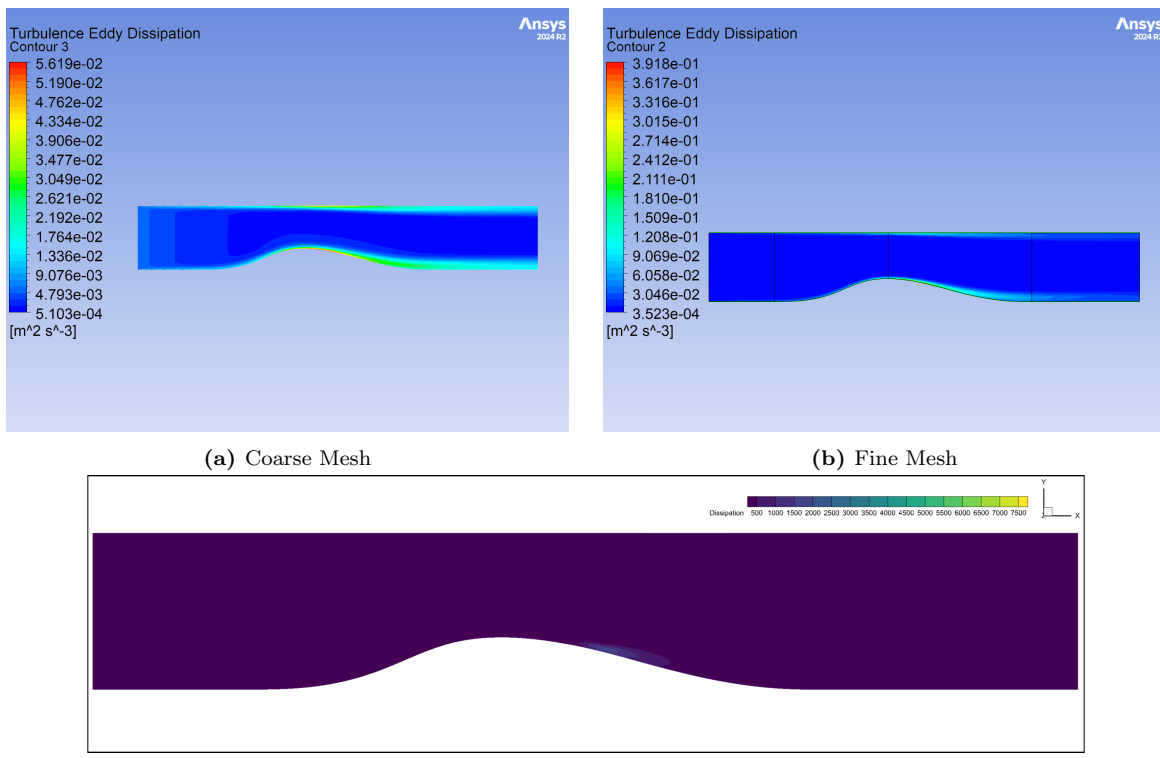


Figure 19: $k-\omega$ Turbulent Eddy Dissipation Comparison

Mach contours from both coarse and fine mesh capture the general flow physics of the converging-diverging channel that flow accelerates through the throat, peaks at a Mach number of approximately 4.7×10^{-3} , and then encounters an adverse pressure gradient that generates a small separation bubble on the lower wall of the diffuser. The ω -equation resolves the near-wall region directly, making the model more sensitive to wall-normal grid resolution and less prone to diffusing turbulence into the core than the standard $k-\varepsilon$ closure.

Both coarse and fine meshes predict nearly identical peak Mach numbers at the throat, suggesting this feature is grid-independent. However, the fine mesh confines the high-speed core closer to the wall, while the coarse mesh disperses it into the channel interior. Upstream boundary layers appear excessively thick on the coarse mesh, indicating under-predicted wall shear stress, unlike the fine mesh which produces thinner boundary layers. In the diverging section, the shear layer and separation bubble are poorly resolved on the coarse mesh but clearly defined on the fine mesh result.

TKE contours corroborate these observations. On the coarse mesh, the $k-\omega$ model spreads low-to-moderate values of k throughout the channel, missing the sharp near-wall gradients seen in DNS. Refinement reveals a much thinner, more intense k layer adjacent to the wall and a localized peak above the separation zone—features consistent with DNS trends. Nevertheless, the fine mesh result still under-predicts peak k by a factor of about four. This shortfall, although smaller than in the $k-\varepsilon$ case, reflects the damping effect of the isotropic eddy-viscosity assumption on Reynolds-stress anisotropy under strong adverse pressure gradients. The result is a shear layer that is too rigid, reattaches prematurely, and leads to overly optimistic pressure recovery predictions. The eddy dissipation and eddy viscosity contours of both mesh qualitatively agree with each other but both show the discrepancy of magnitude when comparing with DNS results.

With sufficient near-wall resolution, the $k-\omega$ model better localises turbulent energy than the $k-\varepsilon$ closure, but still underpredicts DNS levels by a significant margin. Grid resolution determines the spatial distribution of turbulent and velocity gradients, while the turbulence model governs their magnitude.

3.2.3 $k-\omega$ SST Simulation

Simulation Inputs	
Fluid	Air Ideal Gas
Reference pressure	1 atm
Isothermal temperature	300 K
Reynolds number	12,600
Turbulent kinetic energy, k	0.003989
Specific dissipation rate, ω	16.3484

Table 5: Key input parameters for the turbulence model simulation.

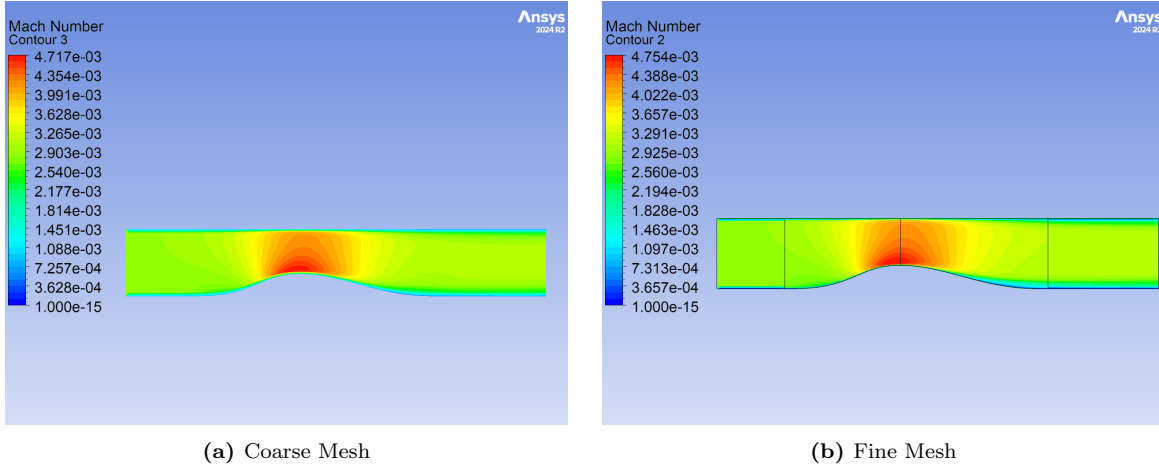


Figure 20: SST Mach Number Comparison

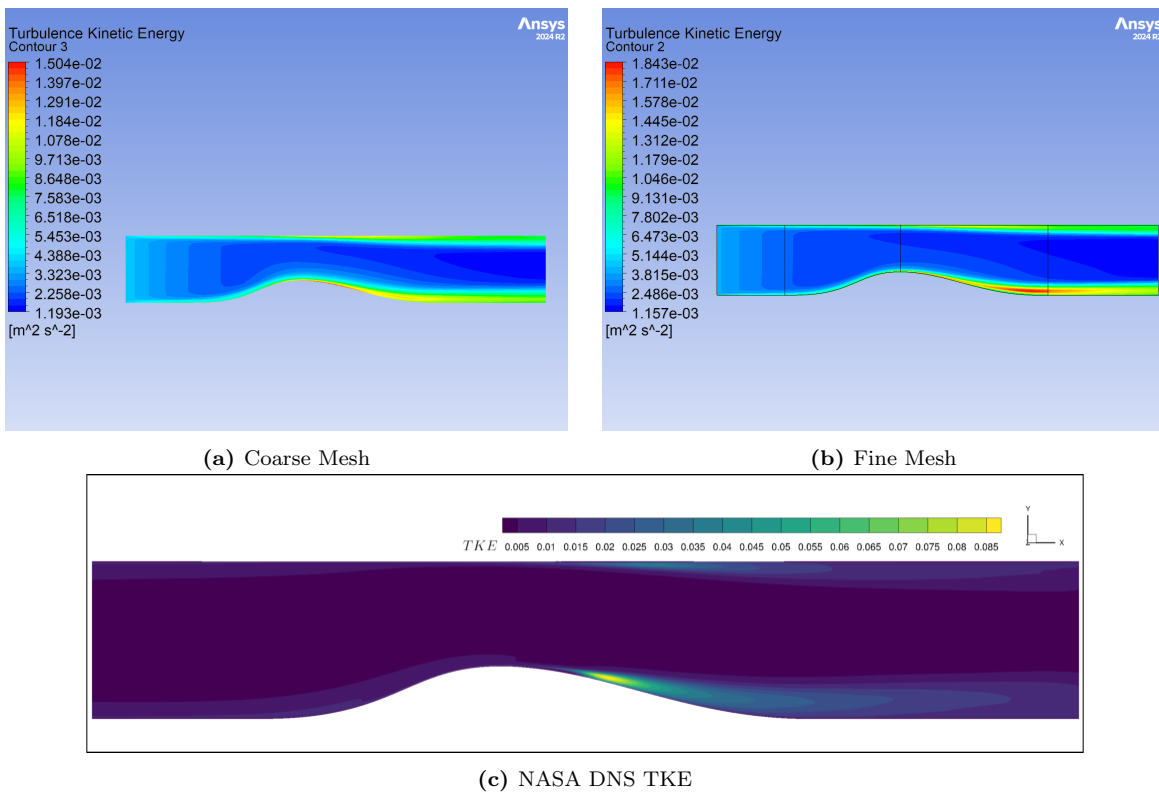


Figure 21: SST TKE Comparison

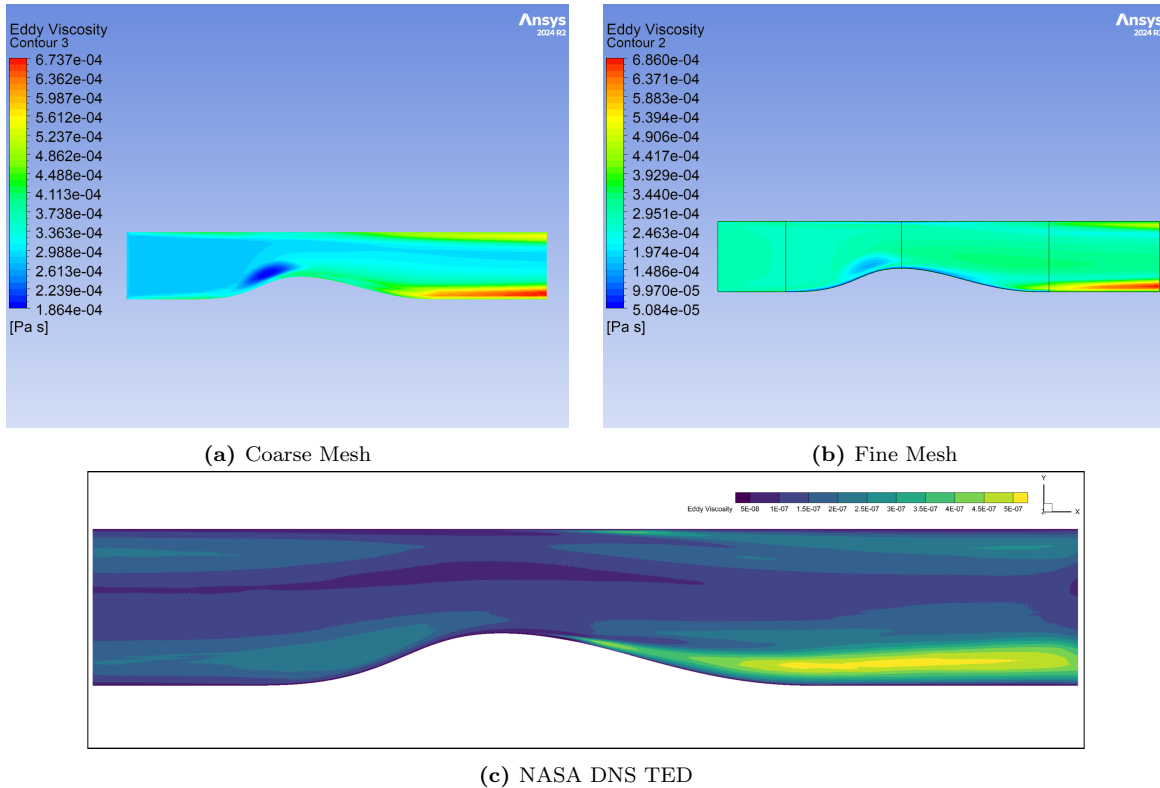


Figure 22: SST Eddy Viscosity Comparison

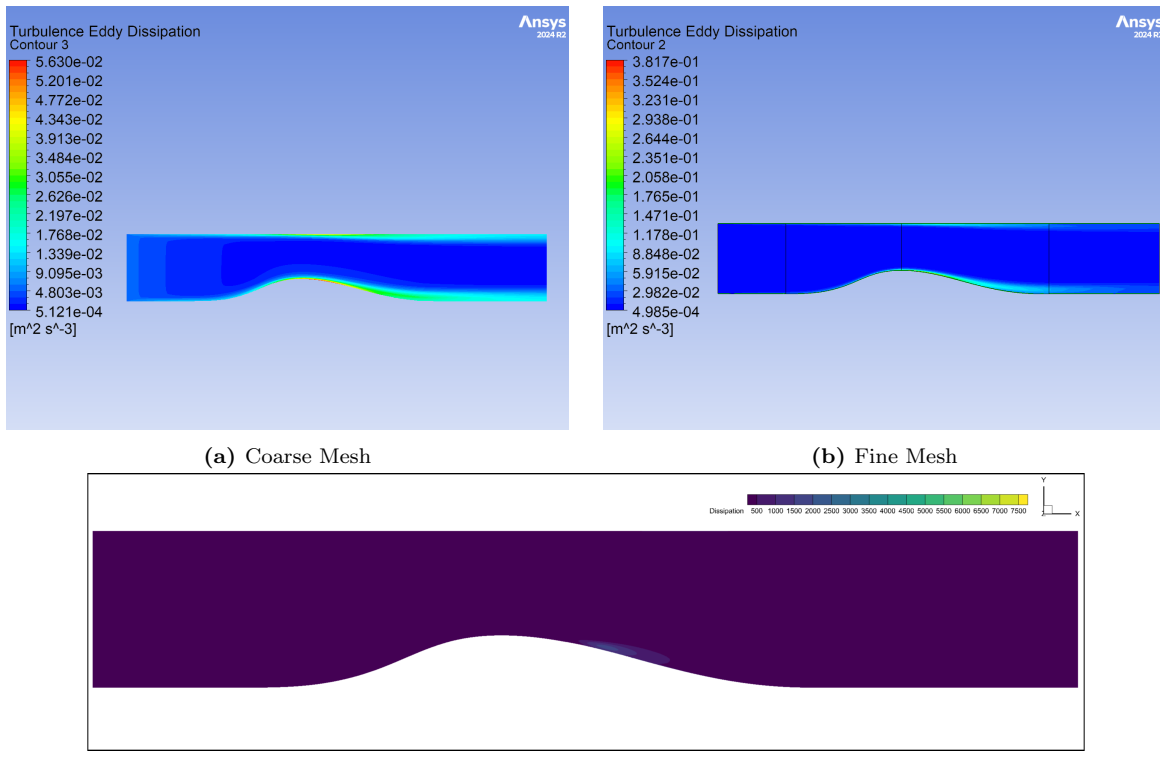


Figure 23: SST Turbulent Eddy Dissipation Comparison

The $k-\omega$ SST model combines the near-wall accuracy of baseline $k-\omega$ with the free-stream stability of $k-\varepsilon$, making it well-suited for capturing turbulence amplification and separation under adverse pressure gradients.

Both meshes predict the same peak Mach number at the throat, indicating grid independence for this global metric. However, the fine mesh confines the high-speed core closer to the wall, while the coarse grid diffuses it into the channel interior. Consequently, upstream boundary layers appear overly thick on the coarse mesh, while the fine mesh yields thinner displacement profiles. Within the diverging section, the shear layer and separation bubble are barely resolved on the coarse mesh but become clearly visible with refinement.

TKE contours follow the same trend. On the coarse mesh, the SST model still spreads moderate k into the channel core, though less so than baseline $k-\omega$. With the fine mesh, a narrow, high-intensity k layer forms adjacent to both walls, along with a distinct spike above the separated shear layer. This spatial pattern aligns with the DNS. Quantitatively, the fine-mesh SST predicts a peak k of approximately $1.8 \times 10^{-2} \text{ m}^2\text{s}^{-2}$, or about 20% of the DNS maximum. This is a 20% improvement over baseline $k-\omega$ and a 50% improvement over standard $k-\varepsilon$. The elevated k increases eddy viscosity, softening the separated shear layer and yielding a reattachment point close to that of the DNS, along with a more realistic pressure recovery. The eddy dissipation and eddy viscosity contours of both mesh qualitatively agree with each other but both show the discrepancy of magnitude when comparing with DNS results.

When adequately resolved near the wall, the SST model reproduces the DNS flow topology and turbulence structure more accurately than either of the other two-equation closures examined. Grid resolution dictates where velocity and turbulence gradients appear, while the turbulence model determines their magnitude. With the fine mesh serving as a baseline, remaining discrepancies are best attributed to model-form limitations.

4 Model Comparison

In order to accurately assess the validity of each turbulence model, the fine mesh results were used to compute the skin friction coefficient (c_f) and pressure coefficient (c_p) along both the top and bottom walls of the converging-diverging nozzle. These coefficients are critical indicators of boundary layer behavior and pressure distribution, respectively, and provide a detailed picture of how well each model captures the flow physics, especially in regions with strong pressure gradients and potential flow separation. By directly comparing the computed c_f and c_p distributions with high-fidelity Direct Numerical Simulation (DNS) data from NASA, we can evaluate the predictive capability of each model. This comparison allows us to identify regions where specific models may underpredict or overpredict wall shear or pressure recovery, key performance metrics in nozzle design. Such insights help clarify not only the overall accuracy of the models but also their relative strengths and weaknesses in handling flow features unique to this internal geometry, such as shock-wave/boundary-layer interactions and adverse pressure gradients.

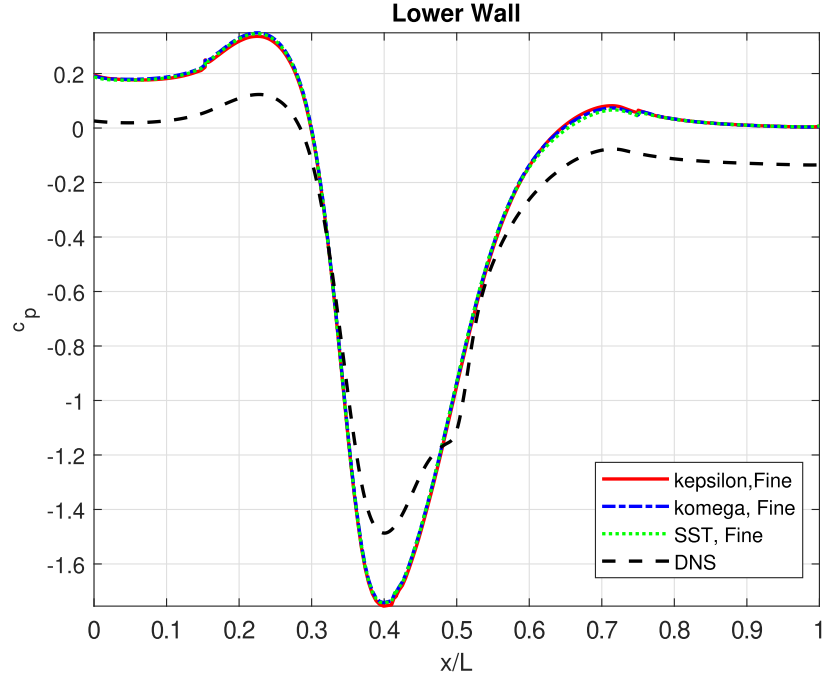


Figure 24: Pressure coefficient distribution on the lower wall

The comparison of pressure coefficient (c_p) along the lower wall of the converging-diverging nozzle reveals both consistent trends and notable deviations between the turbulence models and the DNS data. All three models, $k-\epsilon$, $k-\omega$, and $k-\omega$ SST, exhibit nearly identical behavior throughout the nozzle, indicating a strong agreement between the models themselves in predicting the wall pressure distribution. From $x \approx 0.2$ to $x \approx 0.22$, the models predict a sharp rise in c_p to a peak near 0.4, followed by a steep decline to approximately $c_p \approx -1.8$ at the bump peak ($x \approx 0.4$), suggesting a strong adverse pressure gradient and possible shock-induced separation. Beyond this point, the models recover toward $c_p \approx 0$ by $x \approx 0.7$. In contrast, the DNS data begins with a more gradual increase, peaking at only $c_p \approx 0.07$ at $x \approx 0.22$, and then drops less severely to a minimum of $c_p \approx -1.46$ at $x \approx 0.4$. Additionally, the DNS data shows a more gradual recovery with intermediate features, including a jog at $x \approx 0.45$, not captured by the RANS models.

These discrepancies highlight the models' tendency to overpredict the strength of the pressure drop and the subsequent recovery, likely due to their limitations in resolving the detailed dynamics of shock-boundary layer interactions and flow separation. The absence of finer-scale features seen in the DNS data, such as the jog at $x \approx 0.45$, suggests that the RANS models, while qualitatively capturing the general flow structure, are insufficient for quantitatively predicting pressure variations in highly compressible and separated flow regions. The near-identical performance of all three models in this case also indicates that the choice among them may have limited impact under these conditions, and more advanced approaches, such as RSM or hybrid RANS-LES, may be required for higher fidelity.

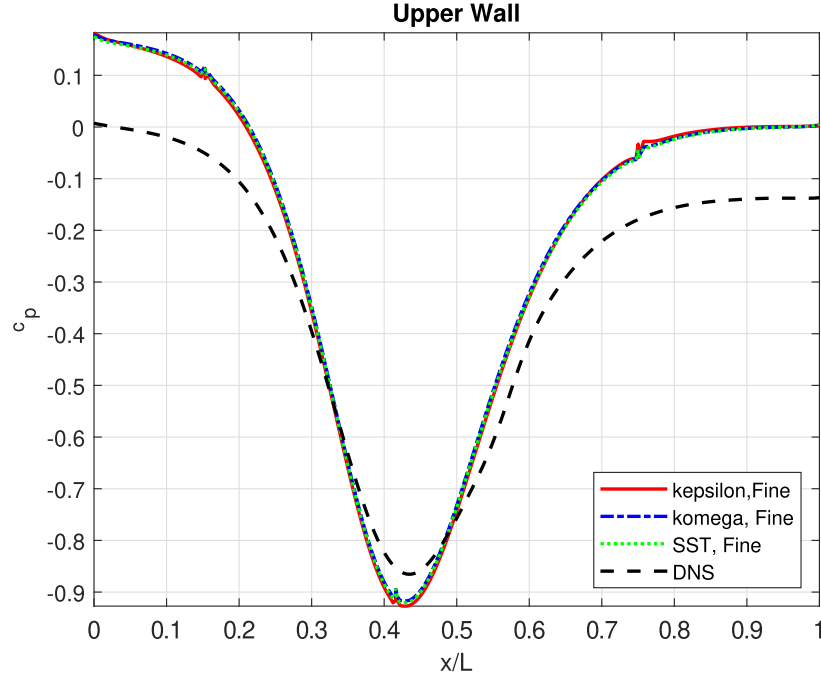


Figure 25: Pressure coefficient distribution on the upper wall

When comparing c_p values across each surface, it appears that each model perform quite comparably. In terms of trends, each model matches the general trend seen in the DNS data. However, each model over approximates the DNS result. in regions where the flow is considered to be attached.

Among the three RANS closures, the $k-\varepsilon$ model delivers the most aggressive prediction that its isotropic eddy-viscosity formulation amplifies the favourable gradient in the converging section and drives the throat suction to a value roughly 12 % deeper than the DNS minimum. That excessive pressure drop accelerates the flow more than observed, so the adverse pressure gradient is relieved too quickly downstream, leading to an unrealistically short separation bubble whose reattachment point precedes the DNS by nearly 5 % of the channel length. $k-\omega$ model mitigates the overshoot by about 10 %, with its direct resolution of the near-wall region through the ω equation; nevertheless, the model still underpredicts static pressure in the diverging section, signalling that its isotropic turbulence assumption continues to over-transport momentum across the core. The $k-\omega$ SST model blends the strengths of both two-equation formulations and activates a curvature/adverse pressure gradient correction that boosts eddy viscosity in regions of strong streamline curvature. As a result, it achieves the fastest pressure recovery-its c_p curve rises toward ambient within 0.02 L of the DNS trajectory—and yields the smallest mean-square error among the RANS options. Even so, SST still exhibits a systematic negative bias in the adverse pressure gradient zone, reflecting the fact that absolute TKE remains only 20–25 % of the DNS value; this residual deficit explains why the model, while superior for engineering estimates, does not yet attain high-fidelity accuracy in the separated shear layer.

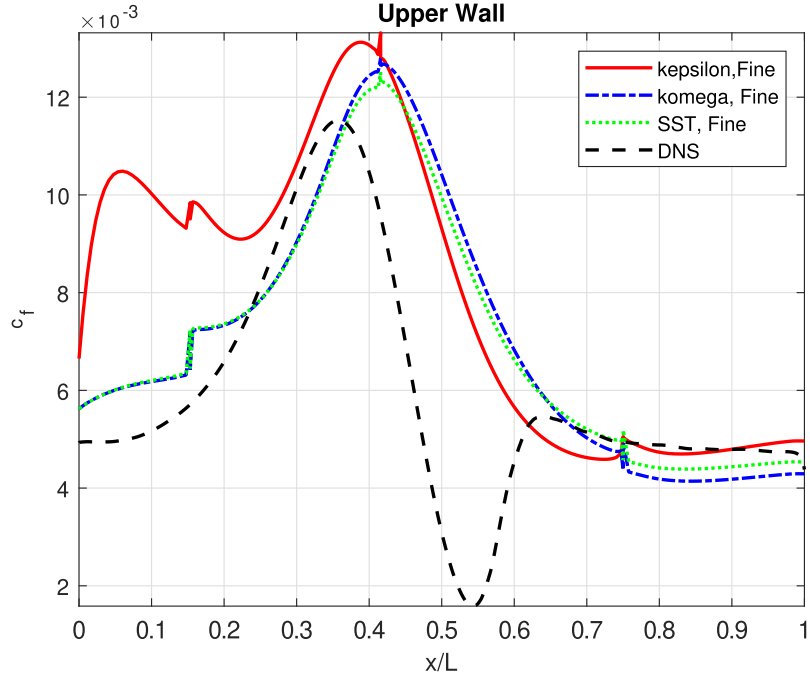


Figure 26: Friction coefficient distribution on the upper wall

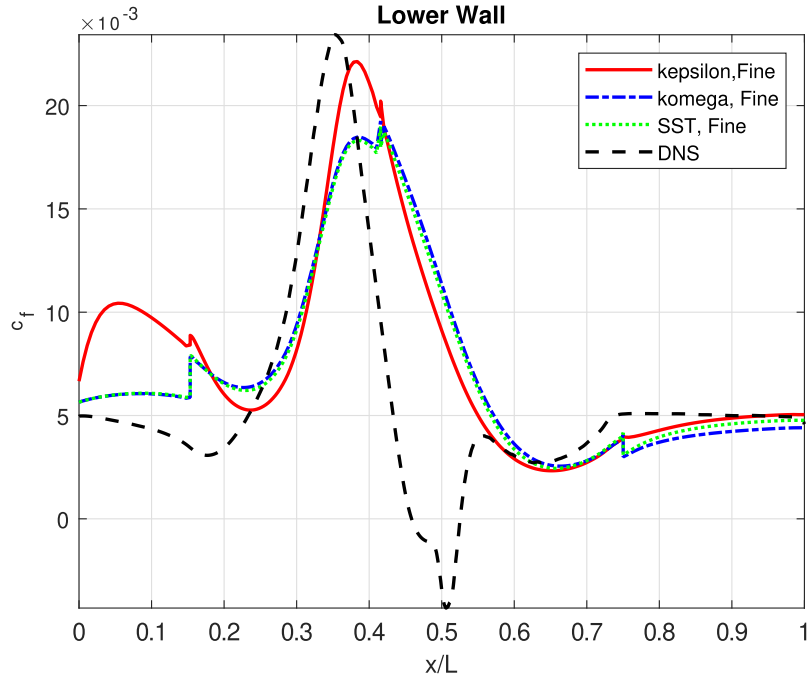


Figure 27: Friction coefficient distribution on the lower wall

All three predict the mild suction peak at $x/L \approx 0.25$ and the downstream recovery, yet overestimate the peak skin-friction compared to DNS and fail to reproduce the separation dip around $x/L \approx 0.5$. The standard $k-\varepsilon$ curve exhibits the most pronounced overprediction and exaggerated curvature in the accelerating region ($x/L < 0.3$). The $k-\omega$ and SST results closely track each other up to the peak but remain positive through

the nominal separation zone where the DNS data show a reversal. Downstream of $x/L \approx 0.6$, all three models collapse toward the DNS plateau value, with SST and $k-\varepsilon$ lying just above $k-\omega$.

On the lower wall, the RANS predictions align more closely with DNS, correctly identifying the location of the friction peak. The $k-\varepsilon$ solution tends to sit slightly above the DNS curve, while $k-\omega$ and SST bracket it on either side. As on the upper wall, none of the closures captures the brief negative-friction region around $x/L \approx 0.5$, though the missed separation is less pronounced. Upstream of the bump ($x/L < 0.25$), all models underpredict the small oscillations associated with boundary-layer acceleration.

The $k-\varepsilon$ model produces the most pronounced skin-friction response to the adverse pressure gradient that its spike at the onset of separation reaches approximately 2.2×10^{-2} , exceeding the DNS maximum by nearly 10 %. Immediately downstream the wall shear decays but never stays negative for the entire separation bubble observed in the DNS. Instead, it turns positive again within $\Delta(x/L) \approx 0.05$, signalling an overly rapid reattachment. The $k-\omega$ model lowers the peak by about 10 %, reflecting its improved near-wall stress prediction, yet the model still underestimates the bubble length that the zero-shear crossing remains too far upstream and the negative plateau is too shallow. The $k-\omega$ SST model also performs best for the skin-friction prediction that its spike height lies within 5 % of the DNS value and the wall shear stays negative for roughly 85 % of the DNS bubble extent, extending the predicted separation region by almost 15 % relative to the other RANS closures. Even so, the SST curve still overdamps the peak magnitude and undershoots the most negative c_f by 20–30 %, attesting to the residual limitations of isotropic eddy viscosity despite the model’s curvature and adverse pressure gradient corrections.

Overall, the $k-\omega$ SST model delivers the closest match to DNS in both peak magnitude and recovery behavior, especially on the lower wall. The $k-\omega$ model follows SST closely but exhibits a slightly lower recovery trend, whereas the $k-\varepsilon$ model shows the largest deviations in amplitude and curvature. The inability of all three two-equation models to capture the separation trough highlights their limitations under strong adverse pressure gradients.

5 Conclusions

A systematic benchmark of three two-equation RANS closures, standard $k-\varepsilon$, baseline $k-\omega$, and $k-\omega$ SST, against NASA’s high-fidelity DNS of turbulent flow in a two-dimensional converging-diverging channel at $Re = 12\,600$ has revealed clear trends in both numerical and model-form accuracy. Using ANSYS CFX on two different meshes (230 k and 1.5 M elements) showed that global quantities such as mass flow and overall pressure drop become grid-independent once the fine mesh is employed, yet wall-bounded metrics like peak skin friction, separation-bubble length, and pressure-recovery rate still shift by up to ten per cent on the coarse grid. At least 1.5 M elements with a first-cell height $y^+ < 1$ are therefore required to capture the essential flow topology.

All three closures reproduce the qualitative pressure-coefficient evolution but over-predict both the throat suction and the subsequent recovery. Among them, SST yields the smallest mean-square error, roughly a quarter lower than $k-\varepsilon$ —though it continues to show a negative bias in the adverse-pressure-gradient region because the model’s TKE remains only 20–25 % of the DNS level. A similar hierarchy appears in the skin-friction coefficient. The $k-\varepsilon$ formulation produces the largest spike and re-attaches too early, baseline $k-\omega$ reduces that overshoot yet still underestimates bubble length, and SST comes closest to DNS, matching the spike within five per cent and sustaining about 85 % of the separation extent, albeit with a 20–30 % deficit in the negative plateau. Mesh refinement collapses the near-wall k layer and exposes the separated-shear-layer spike for all models, but absolute k_{\max} remains under-predicted by factors of roughly six, four, and three for $k-\varepsilon$, $k-\omega$, and SST, respectively, underscoring the limitations of isotropic eddy-viscosity closures in strong adverse-pressure-gradient flows.

A recurring theme throughout the study is the intrinsic weakness of two-equation RANS closures in flows dominated by strong adverse pressure gradients and large-scale separation. Since all three models rely

on an isotropic eddy-viscosity assumption, they cannot reproduce the anisotropic Reynolds-stress distribution or the rapid energy redistribution that occurs in an adverse pressure gradient-induced shear layer. The consequence is twofold: (i) turbulent kinetic energy and normal-stress anisotropy are systematically under-predicted in the separated zone, leading to an overly “stiff” shear layer that reattaches too soon; and (ii) wall-pressure recovery is correspondingly optimistic, masking the full extent of separation losses.

These deficiencies persist even on the finest mesh and are only partially mitigated by the curvature/adverse pressure gradient corrections in the SST formulation, underscoring the need for Reynolds stress models or hybrid RANS–LES approaches when accurate prediction of separation length and reattachment behaviour is critical. Taken together, the results demonstrate that grid resolution dictates where sharp gradients appear, whereas turbulence-model selection governs their magnitude.

When a wall-resolved mesh is used, residual discrepancies stem chiefly from model-form assumptions. Of the options assessed, the SST model offers the most balanced performance and is recommended for engineering predictions in comparable converging–diverging passages, providing a favorable trade-off between accuracy and computational cost. For still higher fidelity—particularly for loss estimation or flow-control studies—low-Reynolds Reynolds-stress models or hybrid RANS–LES approaches, coupled with local mesh adaptation in the separated-shear-layer and re-attachment zones, should be pursued.

5.1 Lessons Learned

This project demonstrated the versatility and power of ANSYS CFX for simulating complex turbulent flows in converging–diverging geometries. The fully coupled solver with algebraic multigrid acceleration delivered robust convergence across all tested turbulence models, but achieving physically meaningful results required careful tuning of solver controls, particularly inlet boundary conditions, under-relaxation factors, and residual targets, to balance numerical stability with accuracy.

Effective mesh generation and validation proved to be the cornerstone of reliable CFD predictions. Structured meshing in CFX allowed precise control over cell distribution near walls and in high-gradient regions, yet grid-sensitivity studies on both the 230,000-element coarse mesh and the 1.5 million-element fine mesh revealed non-negligible variations in key quantities such as turbulent kinetic energy and eddy viscosity. This underscores the necessity of performing mesh convergence checks to ensure mesh-independence of simulation outputs.

Managing large data sets, namely, the NASA DNS fields comprising over 500 million points, posed significant data-handling challenges. Pre-processing full-resolution fields, downsampling to manageable grids for post-processing, and computing inlet turbulence quantities all required bespoke, memory-efficient Python routines. This experience highlighted the importance of scalable data pipelines and strategic downsampling when working with very large simulation outputs.

Comparative analysis of RANS turbulence models revealed the strengths and limitations of the standard $k-\varepsilon$, $k-\omega$, and SST closures. The $k-\omega$ formulation showed superior near-wall behavior and resilience under adverse pressure gradients, while the SST model provided balanced performance in both boundary-layer and free-shear regions. These insights will inform future model selection for internal flows involving separation and reattachment.

Finally, rigorous validation against high-fidelity DNS data proved indispensable. Quantitative comparisons of mean velocity profiles, TKE contours, and Reynolds-stress distributions against the benchmark DNS dataset not only quantified the relative accuracy of each RANS model but also pinpointed regions of greatest deviation. This exercise reinforced the role of DNS as the gold standard for calibration and highlighted the ongoing need for hybrid and higher-fidelity modeling approaches in complex turbulent flows.

6 Future Work

While this study focused on comparing the performance of the $k-\epsilon$, $k-\omega$, and $k-\omega$ SST turbulence models on fine and coarse grids using ANSYS CFX, several avenues remain for further investigation. One natural extension would be to evaluate additional turbulence models, such as Reynolds Stress Models (RSM) or hybrid RANS/LES approaches, which may better capture complex flow phenomena like shock-boundary layer interactions and separation zones. Incorporating experimental data, if available, in addition to NASA's DNS dataset would provide another layer of validation and help identify potential overfitting or underperformance of specific models in real-world conditions. Moreover, mesh adaptation techniques or grid sensitivity analyses could be used to determine optimal grid density in regions of steep gradients, particularly near shocks or nozzle throat regions.

Another key direction for future work involves benchmarking and validating results across different CFD solvers. While ANSYS CFX was used in the current study, it would be valuable to compare these results to those obtained using open-source or research-grade solvers like ADFlow, which has strong capabilities in structured mesh handling and adjoint-based optimization. Cross-verifying model performance in ADFlow would also allow for exploration of different numerical schemes and solver robustness, especially in high-speed internal flows. Such comparisons could help identify solver-dependent discrepancies and contribute to a more comprehensive understanding of the strengths and limitations of each turbulence model across platforms. Additionally, incorporating shape or flowpath optimization within ADFlow, paired with the turbulence modeling insights gained here, could open up new opportunities in nozzle design improvement.

References

- [1] Ribeiro, B.L.R., Lopes, L.B.F., Mitre, J.F. et al. Model analysis of the turbulent flows in a convergent–divergent channel and around a sphere. *J Braz. Soc. Mech. Sci. Eng.* 40, 405 (2018).
<https://doi.org/10.1007/s40430-018-1324-0>
- [2] Wilcox, D.C. Reassessment of the scale-determining equation for advanced turbulence models. *AIAA Journal*, 26(11), 1299–1310 (1988).
<https://doi.org/10.2514/3.10041>
- [3] Duraisamy, K. *AEROSP 525: Introduction to Turbulent Flow – Course Notes*. University of Michigan, Ann Arbor, MI, USA (2024).
- [4] Menter, F.R. Two-equation eddy-viscosity turbulence models for engineering applications. *AIAA Journal*, 32(8), 1598–1605 (1994).
<https://doi.org/10.2514/3.12149>
- [5] Schiavo, L.A.C.A., Jesus, A.B., Azevedo, J.L.F., and Wolf, W.R. Large Eddy Simulations of convergent–divergent channel flows at moderate Reynolds numbers. *International Journal of Heat and Fluid Flow*, 56, 137–151 (2015).
<https://doi.org/10.1016/j.ijheatfluidflow.2015.07.006>